



Cite this: *Chem. Commun.*, 2017, 53, 8284

Received 13th May 2017,
Accepted 16th June 2017

DOI: 10.1039/c7cc03727a

rsc.li/chemcomm

Facile electrospinning formation of carbon-confined metal oxide cube-in-tube nanostructures for stable lithium storage†

Ziang Liu,^{‡a} Ruiting Guo,^{‡a} Jiashen Meng,^a Xiong Liu,^a Xuanpeng Wang,^a Qi Li^{*a} and Liqiang Mai^{ib*ab}

A unique carbon-confined metal oxide cube-in-tube nanostructure is synthesized by a facile precursor-modified electrospinning method with subsequent pyrolysis. This nanostructure has a partly graphitized carbon layer with manganese oxide nanoparticles embedded as the tube and amorphous CoSnO₃ hollow cubes uniformly distributed inside the tube. As a lithium-ion battery anode, this architecture exhibits a high reversible discharge capacity and rate capability.

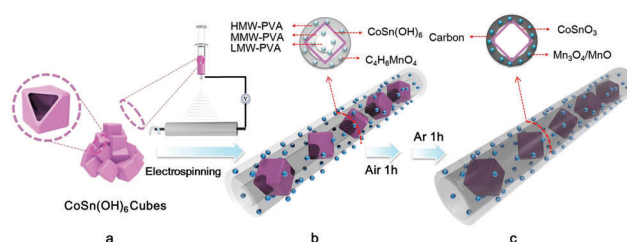
Long lifespan and high energy density rechargeable lithium-ion batteries (LIBs) are widely used in portable electronics owing to their environmental benignity, no memory effect and lightweight.^{1,2} In the past decade, metal oxides as the alloying- and conversion-type anode materials have attracted great attention. Their much higher capacity ($\sim 1000 \text{ mA h g}^{-1}$) compared to that of commercial graphite (372 mA h g^{-1}) would greatly increase the energy density of LIBs.³⁻⁷ However, a large volume variation in charge/discharge processes and a low electronic conductivity cause pulverization, aggregation of active particles and formation of an unstable solid-electrolyte interphase (SEI), leading to a fast capacity decay.⁸⁻¹²

To address these aforementioned problems, researchers have put forward many strategies. Carbon coating has been proved to be a facile and effective method to improve the electronic conductivity.¹³⁻¹⁶ Zhang *et al.* reported that carbon-coated Fe₃O₄ exhibited threefold lithium-storage performance compared to bare Fe₂O₃ at 0.5 C, and the proper carbon coating can also facilitate the formation of a uniform thin SEI layer.¹⁷ To alleviate volume variation, contraction of various hollow structures is the most effective way. In particular, one-dimensional (1D) hollow structures have attracted enormous attention because they can not only buffer

the volume change and inhibit aggregation, but also provide rapid charge transfers in one direction.¹⁸⁻²⁰ Lou *et al.* designed Si/Ge (volume change up to 400%) alloy nanotubes which show greatly improved cycling performance compared to simple Si nanowires and Ge nanowires.²¹ Recently, a new class of conversion/alloying materials (CAMs) which combine the merits of conversion and alloying reactions have attracted increasing attention.²²⁻²⁴ In these materials, when one component reacts with lithium ions, another one can buffer the volume variation and facilitate the structure evolution. As a result, this synergistic effect endows these CAMs with enhanced electrochemical performance.

Herein, we developed a simple precursor-modified electrospinning method to fabricate multilevel hollow cube-in-tube nanostructures. After subsequent pyrolysis, partly graphitized carbon layers connect manganese oxide (conversion mechanism) nanocrystals together, forming stable, high electronic-conductivity tubes. High-capacity amorphous CoSnO₃ (conversion/alloying mechanism) hollow cubes are uniformly anchored inside these tubes, which also improve the tap density. These multilevel hollow structures possess adequate void space and mechanical strength to accommodate volume variation in the charge/discharge processes and hence exhibit excellent lithium storage performance.

The fabrication process of cube-in-tube nanostructures can be divided into three steps approximately (Scheme 1). First, CoSn(OH)₆ hollow nanocubes with uniform size ($\sim 150 \text{ nm}$) and wall thickness



Scheme 1 Schematic illustration of the formation process of cube-in-tube nanostructures. (a) Pre-prepared CoSn(OH)₆ hollow cubes, (b) electrospun gradient PVA nanofibers with CoSn(OH)₆ hollow cubes and manganese acetate uniformly distributed in them and (c) cube-in-tube nanostructures.

^a State Key Laboratory of Advanced Technology for Materials Synthesis and Processing, Wuhan University of Technology, Wuhan 430070, China.
E-mail: qi.li@whut.edu.cn, mlq518@whut.edu.cn

^b Department of Chemistry, University of California, Berkeley, California 94720, USA

† Electronic supplementary information (ESI) available: Experimental details and supplementary figures. See DOI: 10.1039/c7cc03727a

‡ Z. A. Liu and R. T. Guo contributed equally to this work.

(~15 nm) were obtained through a co-precipitation method at room temperature (Fig. S1, ESI†).⁴ Then, the pre-prepared hollow nanocube powder was added into a transparent precursor solution of high-/middle-/low-molecular-weight poly(vinyl alcohol) (HMW/MMW/LMW-PVAs) and manganese acetate for electro-spinning. After that, PVAs were distributed into three layers along the radial direction in the composite fibers, which has been proved in our previous works.^{25,26} Hollow cubes and manganese acetate were spread in the fibers uniformly (Scheme 1b) and a nanotube has not been formed at this stage (Fig. S2a, ESI†). According to Fig. S2d, ESI† all the peaks of these composite fibers in the X-ray powder diffraction (XRD) pattern can be indexed to pure $\text{CoSn}(\text{OH})_6$. The as-prepared nanofibers were then pre-sintered at 300 °C in air for 1 h, forming carbon-confined nanotubes with manganese oxide (Mn_3O_4) spreading in the carbon layers (Fig. S2b, ESI†), while the nanocubes stayed in the center of the nanotubes because of their relatively large volume and high weight (Scheme 1c). The corresponding XRD pattern shows the formation of the Mn_3O_4 phase (Fig. S2e, ESI†). Finally, partly graphitized carbon tubes with manganese oxides embedded in the outer layers and CoSnO_3 hollow cubes uniformly anchored inside the tubes were obtained after sintering at 450 °C under an argon atmosphere for 1 h. The conversion of partial Mn_3O_4 to MnO was also observed in the XRD pattern after the graphitization process, which may result from the reducibility of carbon (Fig. S2f, ESI†). By contrast, when manganese acetate was removed from the precursor solution, the outer nanotube could not be maintained in the sintering processes (Fig. S4, ESI†). Moreover, it is important that the diameter of the nanotubes should well match with the size of the nanocubes to enable the successful fabrication of the nanostructure (Fig. S3, ESI†).

Scanning electron microscopy (SEM) images (Fig. 1a and b) clearly show uniform cube-in-tube structures. The outer part of the as-prepared cube-in-tube nanostructures consists of smooth and continuous carbon-confined manganese oxide nanotubes.

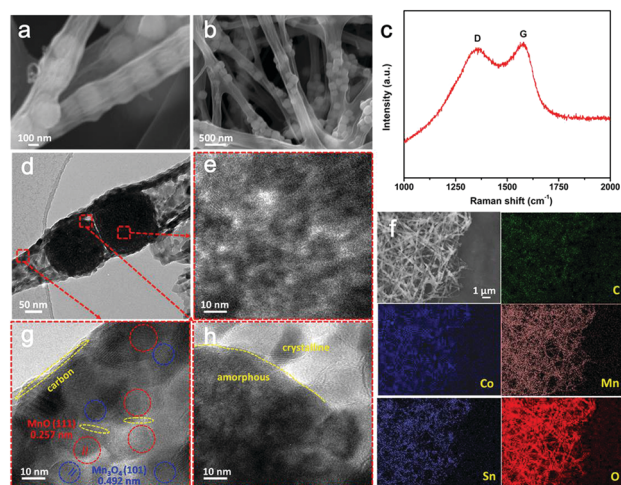


Fig. 1 (a and b) SEM images, (c) Raman spectrum, (d) TEM image, (e, g and h) HRTEM images and (f) EDS elemental mapping images of the cube-in-tube nanostructures containing amorphous CoSnO_3 , manganese oxides and carbon.

Amorphous CoSnO_3 hollow nanocubes are uniformly anchored in the inner part, which provides a higher tap density than that of simplex nanotubes (Fig. S6, ESI†). Energy-dispersive X-ray spectroscopy (EDS) mapping images demonstrate the homogeneous distribution of C, Co, Mn, Sn and O elements (Fig. 1f). The additional inductively coupled plasma-atomic emission spectroscopy (ICP-AES) test shows that the elemental ratio of Co, Sn, and Mn in the test sample (1 : 1.01 : 3) is similar to that in the precursor solution (1 : 1 : 2.93) (Table S1, ESI†). The above results clearly demonstrate the uniform distribution of amorphous CoSnO_3 nanocubes inside the tubes.

In high-resolution transmission electron microscopy (HRTEM) images (Fig. 1e and g), amorphous CoSnO_3 and $\text{MnO}/\text{Mn}_3\text{O}_4$ crystals are observed, which are consistent with the XRD pattern (Fig. S2, ESI†). An obvious boundary between the amorphous phase and the crystal phase (Fig. 1h) suggests that these two phases are independent of each other. The HRTEM image of the nanotubes (Fig. 1g) shows a distinct lattice fringe calculated as 0.257 nm (indicated by red rings) and 0.492 nm (indicated by blue rings), which are attributed to the lattice planes of (111) in MnO and (101) in Mn_3O_4 , respectively. In addition, carbon is found to be uniformly dispersed between these nanoparticles (indicated by yellow curves). The Raman spectrum (Fig. 1c) further indicates that the outer carbon layers are partly graphitized. The mass loss (in air) at 200–600 °C in the thermogravimetric analysis (TGA) test (Fig. S5, ESI†) shows a carbon content of ~4.15 wt% in the cube-in-tube composite. Considering the low carbon content and the low capacity of carbon compared to metal oxides, it is believed that the capacity portion of the amorphous carbon in this composite can be ignored.²⁷

The N_2 adsorption–desorption isotherm shows a type IV curve with the H4 adsorption hysteresis beginning at about $0.5P/P_0$, indicating a mesoporous structure (Fig. 2a). This result corresponds to the pore sizes at about 2.7 and 3.7 nm according to the Barrett–Joyner–Halenda (BJH) analysis (Fig. 2b). The Brunauer–Emmett–Teller (BET) specific surface area is about $34 \text{ m}^2 \text{ g}^{-1}$.

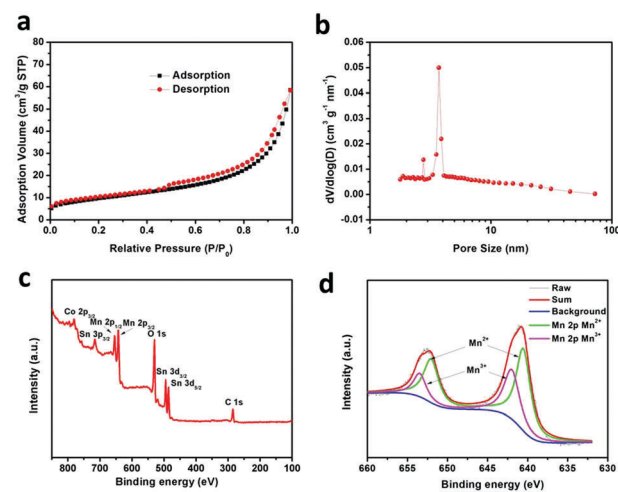


Fig. 2 (a) N_2 adsorption–desorption isotherms and (b) pore size distribution curves of cube-in-tube nanostructures. (c) XPS survey spectrum and (d) the corresponding Mn 2p spectrum of the cube-in-tube nanostructures.

The X-ray photoelectron spectroscopy (XPS) survey spectrum (Fig. 2c) of the cube-in-tube nanostructures indicates the presence of Co, Sn, Mn, O and C, which is consistent with the EDS mapping results. The deconvolution of Mn 2p peaks indicates the presence of Mn²⁺ and Mn³⁺ (Fig. 2d). The doublet peaks at 640.3 eV and 651.9 eV correspond to Mn 2p_{3/2} and Mn 2p_{1/2} in Mn²⁺, while the doublet peaks at 641.4 eV and 653.5 eV correspond to Mn 2p_{3/2} and Mn 2p_{1/2} in Mn³⁺. Moreover, the Mn³⁺/Mn²⁺ ratio measured from the XPS analysis is about 1:2. Therefore, the Mn₃O₄/MnO ratio is estimated to be 1:3. Deconvolutions of Sn 3d and Co 2p suggest the existence of only Sn⁴⁺ and Co²⁺ (Fig. S7, ESI†).

Fig. 3a shows the initial three cyclic voltammetry (CV) scans. In the initial cycle, obvious reduction peaks appeared at about 0.78 V, 0.63 V and 0.10 V and disappeared in the following cycles, which are probably ascribed to the reduction of Mn³⁺ to Mn²⁺, the reduction of Sn⁴⁺ to Sn⁰ and formation of the SEI film.^{28,29} The reduction of Mn²⁺ to Mn⁰ and Co²⁺ to Co⁰ appeared at 0.2 V and 1.04 V in the first scan and shifted to 0.30 V and 1.25 V in the following cycles.^{29,30} From the second cycle, two pairs of stable redox peaks appeared, which are located at 1.25 V/2.10 V and 0.35 V/1.35 V. These redox peaks can be ascribed to the conversion reactions of Co⁰/Co²⁺ and Mn⁰/Mn²⁺.^{28–32} A broad cathodic band extending to 0 V and the corresponding anodic peak at 0.55 V can be ascribed to the alloying/de-alloying reaction of Sn.^{0,33,34} The second and third

CV curves almost overlapped, indicating a highly reversible nature of the electrochemical reactions in the cube-in-tube nanostructures containing amorphous CoSnO₃, manganese oxides and carbon.

The rate capability was evaluated with the current densities ranging from 0.1 to 5 A g⁻¹ (Fig. 3b). This cube-in-tube structure delivers average discharge capacities of 960, 796, 621, 484, 374 and 301 mA h g⁻¹ at current densities of 0.1, 0.2, 0.5, 1, 2 and 5 A g⁻¹. When the current density returns to 0.1 A g⁻¹, the discharge capacity returns to 1081 mA h g⁻¹, indicating a high capacity recovery rate of over 100%. Moreover, the charge/discharge curve at different current densities (Fig. 3d) shows small polarization of this active material. Furthermore, low current cycling performance shows an initial discharge capacity of 1296 mA h g⁻¹ at a current density of 0.1 A g⁻¹, and 1071 mA h g⁻¹ was obtained after 50 cycles (Fig. 3c). The capacity increases after 20 cycles, which may be owing to the anode material activation and the decrease of charge transfer resistance (*R*_{ct}) during cycling (Fig. S8, ESI†). Furthermore, this cube-in-tube nanostructure shows an outstanding cycling stability at a high current density of 2 A g⁻¹ (Fig. 3e). The initial discharge capacity is 463 mA h g⁻¹ and a capacity of 368 mA h g⁻¹ is retained after 1500 cycles. The SEM image of the cube-in-tube nanocomposites after the cycling test indicates that the structure of hollow nanocubes and nanotubes has been retained well, implying the high stability of the structure (Fig. S9, ESI†).

The excellent cycling stability and rate capability can be attributed to the merits of the design of this unique structure. First, partially graphitized carbon layers generated by *in situ* pyrolysis form a continuous conductive layer with manganese oxide nanocrystals uniformly embedded in carbon layers, which can inhibit the aggregation of manganese oxides and greatly increase the electronic conductivity of the anode materials. The thin carbon layer on the surface also benefits the axial electron transfer and strengthens the mechanical stability of the nanotubes, which greatly benefits the rate performance. Moreover, hollow nanocubes and stable nanotubes provide adequate void space and mechanical strength to buffer volume variation during the charge/discharge processes, which enhance the long-term cycling stability (Table S2, ESI†).

In conclusion, a unique cube-in-tube nanostructure is synthesized *via* a facile approach of precursor-modified electrospinning and pyrolysis. As the anode material for LIBs, the cube-in-tube nanostructure of amorphous CoSnO₃, manganese oxides and carbon composites delivers a reversible capacity of 368 mA h g⁻¹ over 1500 cycles even at 2 A g⁻¹. These unique cube-in-tube nanostructures successfully combine the merits from the stability of carbon-confined nanotubes, the high capacity of nanocubes and the hollow structure which efficiently buffers the volume variation, providing a new strategy to enhance the lithium storage performance of metal oxides.

We gratefully acknowledge the National Key Research and Development Program of China (2016YFA0202603), the National Basic Research Program of China (2013CB934103), the Programme of Introducing Talents of Discipline to Universities (B17034), the National Natural Science Foundation of

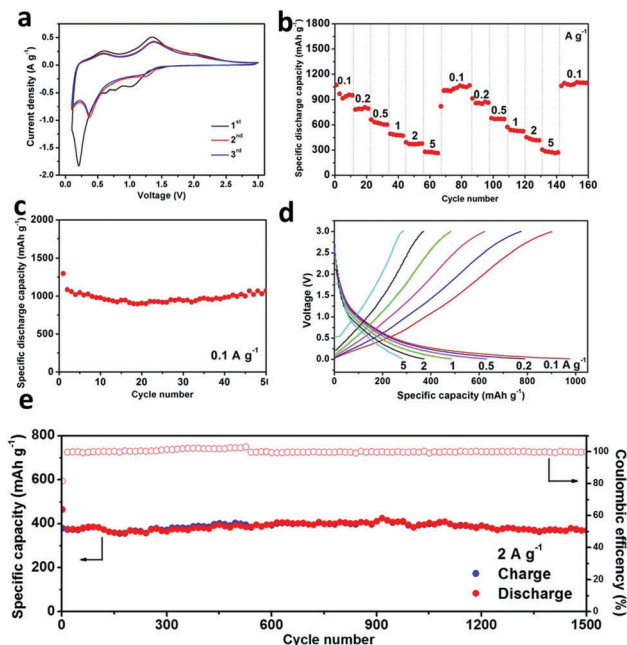


Fig. 3 Electrochemical performance of the cube-in-tube nanostructures containing amorphous CoSnO₃, manganese oxide and the carbon composite. (a) The first three consecutive CV cycles were tested at a scan rate of 0.2 mV s⁻¹ in a potential range from 0.01 to 3.0 V vs. Li⁺/Li. (b) Rate performance tested at the current densities ranging from 0.1 to 0.2, 0.5, 1, 2 and 5 A g⁻¹. (c) Cycling performance tested at the current density of 0.1 A g⁻¹. (d) The charge/discharge curves at various current densities. (e) Cycling performance and Coulombic efficiency tested at the current density of 2 A g⁻¹.

China (51521001), the National Natural Science Fund for Distinguished Young Scholars (51425204), and the Fundamental Research Funds for the Central Universities (WUT: 2016III001, 2017IVA100, 2017III009, 2017III040). We are grateful to Bichao Xu and Pei Zhang of the Core Facility and Technical Support, Wuhan Institute of Virology for her technical support in transmission electron microscopy. Prof. Liqiang Mai gratefully acknowledged financial support from the China Scholarship Council (No. 201606955096).

Notes and references

- 1 P. G. Bruce, B. Scrosati and J. M. Tarascon, *Angew. Chem., Int. Ed.*, 2008, **47**, 2930–2946.
- 2 G. Zhou, F. Li and H.-M. Cheng, *Energy Environ. Sci.*, 2014, **7**, 1307–1338.
- 3 Z. Cai, L. Xu, M. Yan, C. Han, L. He, K. M. Hercule, C. Niu, Z. Yuan, W. Xu, L. Qu, K. Zhao and L. Mai, *Nano Lett.*, 2015, **15**, 738–744.
- 4 Z. Wang, Z. Wang, W. Liu, W. Xiao and X. W. Lou, *Energy Environ. Sci.*, 2013, **6**, 87–91.
- 5 G. L. Xu, Y. F. Xu, H. Sun, F. Fu, X. M. Zheng, L. Huang, J. T. Li, S. H. Yang and S. G. Sun, *Chem. Commun.*, 2012, **48**, 8502–8504.
- 6 J. Sun, D. Li, Y. Xia, X. Zhu, L. Zong, Q. Ji, Y. A. Jia and D. Yang, *Chem. Commun.*, 2015, **51**, 16267–16270.
- 7 H. G. Wang, C. Yuan, R. Zhou, Q. Duan and Y. Li, *Chem. Eng. J.*, 2017, **316**, 1004–1010.
- 8 D. Yu, C. Chen, S. Xie, Y. Liu, K. Park, X. Zhou, Q. Zhang, J. Li and G. Cao, *Energy Environ. Sci.*, 2011, **4**, 858–861.
- 9 J. Zhou, Y. Lan, K. Zhang, G. Xia, J. Du, Y. Zhu and Y. Qian, *Nanoscale*, 2016, **8**, 4903–4907.
- 10 M. Feng, S. Wang, J. Yang and B. Zhang, *J. Mater. Chem. A*, 2016, **4**, 18524–18531.
- 11 X. Hu, G. Zeng, J. Chen, C. Lu and Z. Wen, *J. Mater. Chem. A*, 2017, **5**, 4535–4542.
- 12 H. G. Wang, Y. Zhou, Y. Shen, Y. Li, Q. Zuo and Q. Duan, *Electrochim. Acta*, 2015, **158**, 105–112.
- 13 X. W. Lou, C. M. Li and L. A. Archer, *Adv. Mater.*, 2009, **21**, 2536–2539.
- 14 H. Li and H. Zhou, *Chem. Commun.*, 2012, **48**, 1201–1217.
- 15 Y. Wang, L. Zhang, Y. Wu, Y. Zhong, Y. Hu and X. W. Lou, *Chem. Commun.*, 2015, **51**, 6921–6924.
- 16 X. Wang, C. Niu, J. Meng, P. Hu, X. Xu, X. Wei, L. Zhou, K. Zhao, W. Luo, M. Yan and L. Mai, *Adv. Energy Mater.*, 2015, **5**, 1500716.
- 17 W.-M. Zhang, X.-L. Wu, J.-S. Hu, Y.-G. Guo and L.-J. Wan, *Adv. Funct. Mater.*, 2008, **18**, 3941–3946.
- 18 Y. Zhao and L. Jiang, *Adv. Mater.*, 2009, **21**, 3621–3638.
- 19 Z. Yu, L. Tetard, L. Zhai and J. Thomas, *Energy Environ. Sci.*, 2015, **8**, 702–730.
- 20 H. G. Wang, S. Yuan, D.-L. Ma, X.-B. Zhang and J.-M. Yan, *Energy Environ. Sci.*, 2015, **8**, 1660–1681.
- 21 W. Xiao, J. Zhou, L. Yu, D. Wang and X. W. Lou, *Angew. Chem., Int. Ed.*, 2016, **55**, 7427–7431.
- 22 W. Xie, S. Li, S. Wang, S. Xue, Z. Liu, X. Jiang and D. He, *ACS Appl. Mater. Interfaces*, 2014, **6**, 20334–20339.
- 23 P. Lian, S. Liang, X. Zhu, W. Yang and H. Wang, *Electrochim. Acta*, 2011, **58**, 81–88.
- 24 D. Bresser, S. Passerini and B. Scrosati, *Energy Environ. Sci.*, 2016, **9**, 3348–3367.
- 25 C. Niu, J. Meng, X. Wang, C. Han, M. Yan, K. Zhao, X. Xu, W. Ren, Y. Zhao, L. Xu, Q. Zhang, D. Zhao and L. Mai, *Nat. Commun.*, 2015, **6**, 7402.
- 26 J. Meng, C. Niu, X. Liu, Z. Liu, H. Chen, X. Wang, J. Li, W. Chen, X. Guo and L. Mai, *Nano Res.*, 2016, **9**, 2445–2457.
- 27 K. Chang, W. Chen, L. Ma, H. Li, H. Li, F. Huang, Z. Xu, Q. Zhang and J. Y. Lee, *J. Mater. Chem.*, 2011, **21**, 6251–6257.
- 28 J. Liang, X. Y. Yu, H. Zhou, H. B. Wu, S. Ding and X. W. Lou, *Angew. Chem., Int. Ed.*, 2014, **53**, 12803–12807.
- 29 Y. Xia, Z. Xiao, X. Dou, H. Huang, X. Lu, R. Yan, Y. Gan, W. Zhu, J. Tu, W. Zhang and X. Tao, *ACS Nano*, 2013, **7**, 7083–7092.
- 30 Y. Liu, C. Mi, L. Su and X. Zhang, *Electrochim. Acta*, 2008, **53**, 2507–2513.
- 31 J. Jiang, J. Liu, R. Ding, X. Ji, Y. Hu, X. Li, A. Hu, F. Wu, Z. Zhu and X. Huang, *J. Phys. Chem. C*, 2010, **114**, 929–932.
- 32 Z. Bai, X. Zhang, Y. Zhang, C. Guo and B. Tang, *J. Mater. Chem. A*, 2014, **2**, 16755–16760.
- 33 C. Xu, J. Sun and L. Gao, *J. Mater. Chem.*, 2012, **22**, 975–979.
- 34 V. Etacheri, G. A. Seisenbaeva, J. Caruthers, G. Daniel, J.-M. Nedelec, V. G. Kessler and V. G. Pol, *Adv. Energy Mater.*, 2015, **5**, 1401289.